

Article

Effects of Crystalline Diamond Nanoparticles on Silicon Thin Films as an Anode for a Lithium-Ion Battery

Yonhua Tzeng *, Cheng-Ying Jhan, Shi-Hong Sung and Yu-Yang Chiou

Institute of Microelectronics, National Cheng Kung University, Tainan 70101, Taiwan;
q18101505@gs.ncku.edu.tw (C.-Y.J.); q16111253@gs.ncku.edu.tw (S.-H.S.); q16121135@gs.ncku.edu.tw (Y.-Y.C.)
* Correspondence: tzengyo@mail.ncku.edu.tw

Abstract: Crystalline diamond nanoparticles which are 3.6 nm in size adhering to thin-film silicon results in a hydrophilic silicon surface for uniform wetting by electrolytes and serves as a current spreader for the prevention of a local high-lithium-ion current density. The excellent physical integrity of an anode made of diamond on silicon and the long-life and high-capacity-retention cycling performance are thus achieved for lithium-ion batteries. A specific capacity of 1860 mAh/g(si) was retained after 200 cycles of discharge/charge at an areal current density of 0.2 mA/cm². This is compared to 1626 mAh/g(si) for a thin-film-silicon anode without the additive of diamond nanoparticles.

Keywords: lithium-ion battery; thin film; silicon; anode; diamond; electrolyte wetting

1. Introduction

Rapid development in electric vehicles, renewable energy, high-performance computing, and mobile electronic devices needs high-performance energy storage devices [1–3]. Graphite is the predominant anode material for the most popular mobile energy storage devices of lithium-ion batteries (LIBs), although the specific capacity (372 mAh/g) of graphite is not as high as desirable. Silicon (Si) offers a high theoretical specific capacity (3579 mAh/g for crystalline Li₁₅Si₄) and a relatively low discharge voltage (about 0.4 V vs. Li/Li⁺), making it an attractive candidate for next-generation anode materials for high-energy-density LIBs [4]. However, the low electrical conductivity of silicon and its large volume expansion due to alloying with lithium (about 400%) adversely affect the charge-discharge cycling stability and electrochemical performance of silicon-based anodes [5,6]. Many efforts were made to overcome barriers against the wide adoption of silicon-based anodes. Focus has been on the reduction of the silicon size [7], hybridization [8], and novel structures [9]. Si-based nanoparticles [10], nanowires [11], nanotubes [12], and thin films [13] represent nanoscale structures for the improved cycling stability of silicon-based anodes. Silicon thin films have garnered special attention due to their ease of fabrication, low chemical residue, and precise stoichiometry. A flexible silicon thin-film electrode is especially welcome and suitable for wearable electronics.

Qiu et al. [14] reported Si-thin-film-based LIBs fabricated by the RF magnetron sputtering of amorphous carbon/silicon/carbon/silicon multi-layer thin film structures. An electrode with an initial discharge specific capacity of 1888.74 mAh/g was reported to retain a specific capacity of 1243.56 mAh/g after 150 cycles of discharge/charge.

Liu et al. [15] inserted silver nanoparticles (AgNPs) between RF-sputtered amorphous Si thin films. An anode with the densest AgNPs insertion reached 1250 mAh/g at 10 C with 46% capacity retention. The results demonstrated the feasibility of multi-layer thin-film-silicon anodes by interfacial engineering.

In this study, we fabricated silicon thin films of about a 100 nm thickness by thermal evaporation on copper foils. Single-crystal diamond nanoparticles of a 3.6 nm size in water suspension were attached to the silicon surface by ultrasonication. These processes repeated twice to make a two-layer Si/D/Si/D anode of a total thickness of about 200 nm.



Citation: Tzeng, Y.; Jhan, C.-Y.; Sung, S.-H.; Chiou, Y.-Y. Effects of Crystalline Diamond Nanoparticles on Silicon Thin Films as an Anode for a Lithium-Ion Battery. *Batteries* **2024**, *10*, 321. <https://doi.org/10.3390/batteries10090321>

Academic Editors: Zhenbo Wang, Tingfeng Yi and Gang Sun

Received: 16 August 2024

Revised: 5 September 2024

Accepted: 6 September 2024

Published: 11 September 2024



Copyright: © 2024 by the authors. Licensee MDPI, Basel, Switzerland. This article is an open access article distributed under the terms and conditions of the Creative Commons Attribution (CC BY) license (<https://creativecommons.org/licenses/by/4.0/>).

The diamond surface layer and interfacial layer resulted in a uniform lithium ion current density, which in turn reduced hot spots, where the local high-lithium-ion current density induces excessive internal stress, resulting in the fracture of the silicon thin films. The diamond nanoparticles' decoration further improves the hydrophilicity of the silicon surface for uniform wetting by water-based electrolyte to form a uniform and stable solid-electrolyte interphase (SEI) on the surface of the anode. The thin-film silicon-based anode retains excellent physical integrity with the reduced exposure of the fresh silicon surface due to the fracture of the silicon films. Thinner and more uniform SEI is formed, leaving electrolyte better preserved for the cycling operation of the battery.

2. Materials and Methods

Silicon films and Si/D/Si/D multilayer films were prepared by thermal evaporation deposition. The process utilized n-type crystalline silicon (purity 99.999%) as the evaporation source and copper foils (diameter 14 mm) as the current collectors. Copper foils were cleaned with acetone and alcohol before the deposition of silicon films.

The deposition process was carried out at a background pressure of 3×10^{-6} torr. The deposition rate for the Si films was 0.4–0.5 nm/min, and the deposition was conducted at 200 °C substrate temperature.

A 200 nm-thick silicon film was deposited on a copper foil and used as a reference anode for a lithium-ion battery. For Si/D/Si/D multilayer films, a 100 nm-thick silicon film was first deposited on a copper foil. The silicon film was immersed in a water solution containing 3.6 nm diamond particles in an ultrasonic agitator. The solution was stirred at 60 rpm for 5 min for uniform dispersion of the diamond nanoparticles on the silicon film. Excess diamond particles were removed by rinsing the sample surface with methanol. The electrode was then dried at 100 °C. The same process repeats when multi-layer structures were made.

Details of the fabrication of coin cells and the materials' characterization have been presented in prior publications. Please refer to references [16–20].

3. Results

Figure 1 shows schematic diagrams of (top) Si and (bottom) Si/D/Si/D thin-film anode structures. The thin-film silicon anode is deposited on a copper foil current collector by thermal evaporation, with a total thickness of 200 nm. In addition, the silicon–diamond composite film was deposited with an initial 100 nm silicon film, followed by immersing the electrode in a 3.6 nm nano-diamonds (NDs) suspension in water and using ultrasonic agitation to evenly distribute the nano-diamonds (NDs) on the surface of the silicon film. After drying on a heated plate, another 100 nm silicon film was deposited, and the 3.6 nm diamond film was dispersed on the silicon anode again using the same method.

We use this schematic diagram to illustrate the effect of nano-diamonds (NDs) on the uniform lithiation of the thin-film electrode. The red line represents the pathway of the lithium ions, and the blue diamond-shaped marks represent nano-diamond (ND) particles. In samples without a diamond layer, uneven lithiation during the cycling electrochemical process led to excessive reactions in some local areas, causing the continuous cracking of the thin film and regeneration of the SEI layer at those locations. The severe deformation of the local silicon layer can lead to issues such as the fracture of the active silicon material and electrolyte consumption by the formation of SEI on the newly exposed silicon surface.

Figure 2 displays the scanning electron microscope (SEM) images of anodes made of silicon thin films and Si/D/Si/D thin films. Clustered silicon grains can be seen on the surface of the silicon anode. Nevertheless, except local silicon clusters, the surface morphology appears to be smoother for the silicon anode than the one with diamond nanoparticles on the silicon surface and at the interface between the two silicon layers.

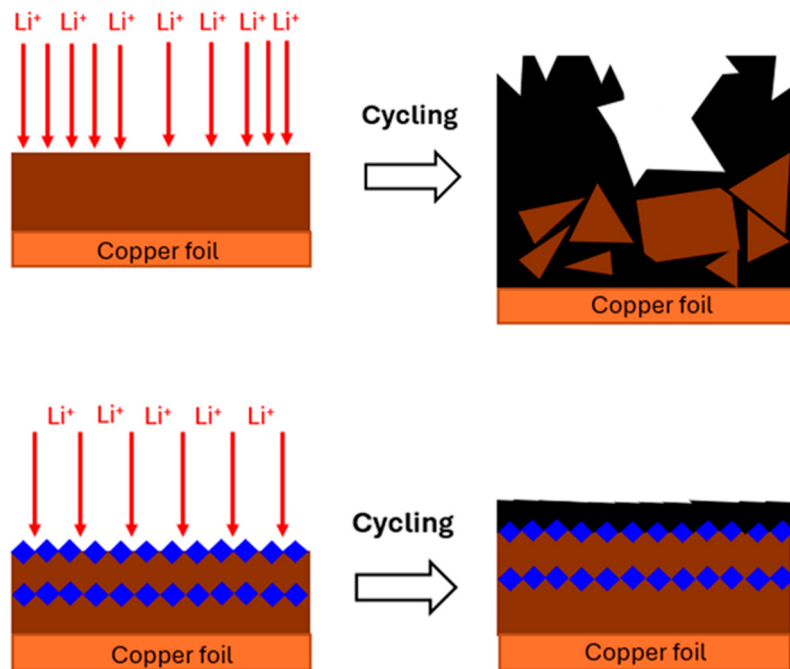


Figure 1. Schematic of the thin-film anodes showing the effects of nano-diamonds (NDs) on the uniform lithiation of the anode made of (top) Si and (bottom) Si/D/Si/D. Red arrows represent the transportation of lithium ions. Blue diamond shape represents nano-diamond (ND) particles. The black area represents SEI layers. Samples without diamond layers exhibited structural instability during cycling, leading to drastic changes in local and overall thickness of the anode.

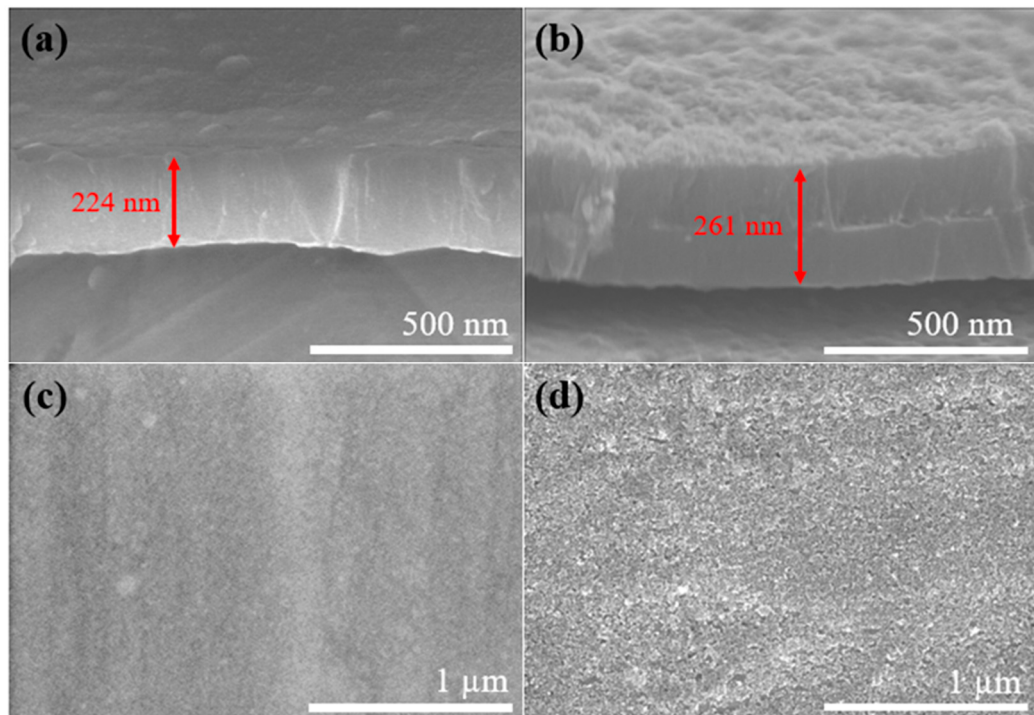


Figure 2. SEM cross-sectional images of (a) Si anode and (b) Si/D/Si/D anode; SEM top-view images of the (c) Si anode and (d) Si/D/Si/D anode.

Figure 2a shows a thermal evaporation deposited silicon anode with a thickness of approximately 224 nm, while Figure 2b illustrates the layered Si/D/Si/D thin-film electrode. The rough surface morphology of the Si/D/Si/D anode might be attributed to

the thicker anode. Since the thicker the silicon anode is, the worse the cycling performance is, the adverse effect of being a slightly thicker Si/D/Si/D anode than that of the Si anode will not affect the conclusion of the performance comparison as long as the thicker Si/D/Si/D anode performs better.

Compared to the characteristic Raman peak shown in Figure 3 of the crystalline silicon at 520 cm^{-1} , the characteristic silicon peak of the deposited silicon thin film is at a lower wavenumber of 493 cm^{-1} . This is due to the lower crystallinity of the deposited silicon thin film. Additionally, the red shift of the characteristic peak is consistent with the characteristics of the small-grain-sized polycrystalline silicon. The silicon thin films are amorphous or, at best, nanocrystalline [21,22].

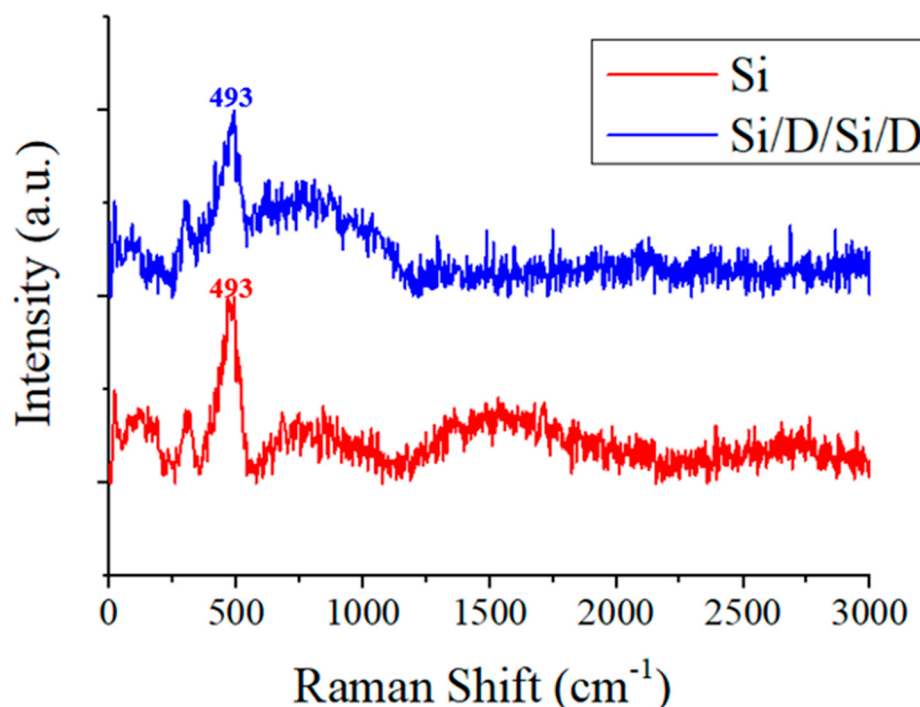


Figure 3. Raman spectra of a Si anode and a Si/D/Si/D anode.

Due to the superior cycling performance of the diamond-on-silicon anode, we conducted cyclic voltammetry (CV) tests on both anodes, i.e., silicon and Si/D/Si/D films, to understand their electrochemical performance. The results are shown in Figure 4.

The cathodic peak below 0.3 V is related to the formation of a series of amorphous phases of Li_xSi . It is worth noting that during the first charge–discharge cycle, the reduction peaks of the Si film at 0.22 V and 0.07 V are relatively unstable, as shown in Figure 4a. This phenomenon may be attributed to the uneven charging and discharging caused by different-sized amorphous silicon particles on the copper foil. Additionally, the reaction peak (0.44 V) of lithium ions migrating from the silicon anode in the first, the second, and the third scans of the Si film is inconsistent, indicating the poor reversibility of the reaction in this sample [23,24].

On the other hand, for the Si/D/Si/D anode, Figure 4b shows that the characteristic peaks of the sample do not change as much as those for the silicon anode with different scans. The almost identical CV graphs of the three scans corresponding to the first three cycles indicate good electrochemical stability and suggest uniform alloying and de-alloying processes.

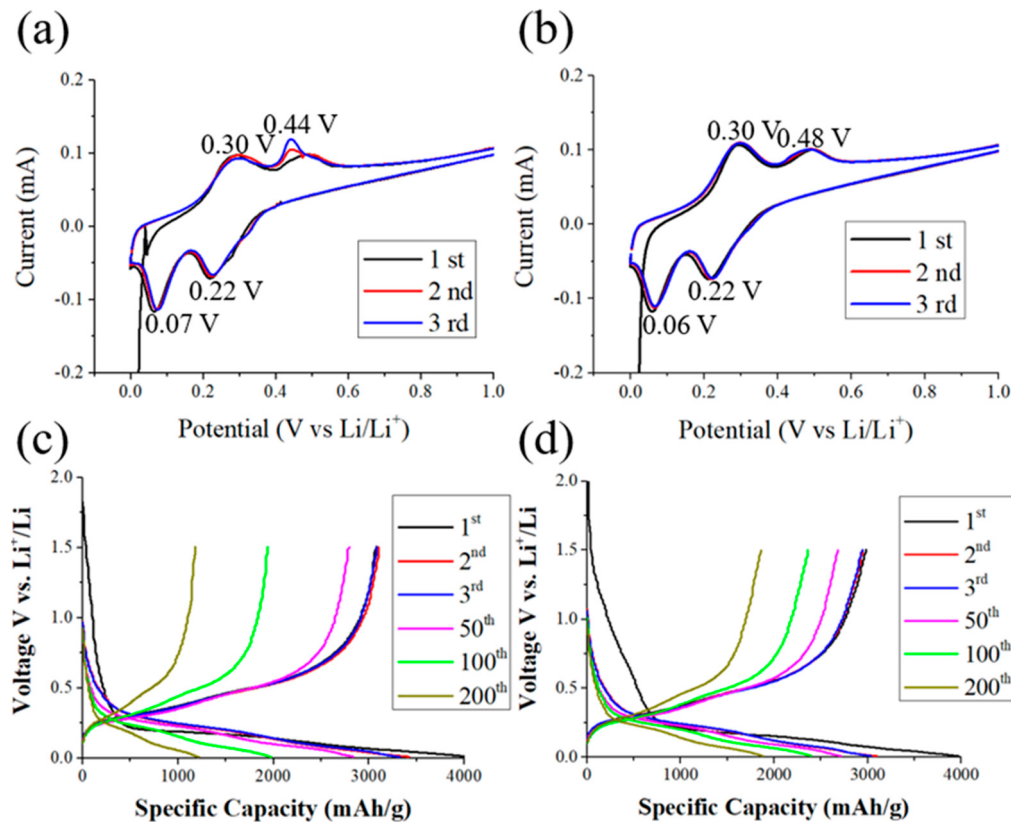


Figure 4. CV curves of (a) Si anode and (b) Si/D/Si/D anode at a scan rate of 0.05 mV/s. Charge–discharge curves of several cycle numbers for the (c) Si anode and (d) Si/D/Si/D anode.

We tested both electrodes using a battery charge–discharge system in a voltage window between 0.01 V and 1.50 V and at a current density of 0.05 mA/cm². The reversible capacities of the Si anode and the Si/D/Si/D anode for the first cycle were 0.143 mAh/cm² (3077 mAh/g (si)) and 0.140 mAh/cm² (2983 mAh/g (si)), respectively. In the first cycle, more SEI layers were observed in the Si/D/Si/D film during the initial electrochemical process. This is possibly due to the increase in the specific surface area of the rough electrode surface caused by diamond nanoparticles, leading to more initial SEI formation. However, the initial Coulombic efficiency of the Si/D/Si/D anode (75.1%) is comparable to that of the silicon anode (76.4%), indicating that the Si/D/Si/D structure can provide both a uniform and stable lithium ion transport path and a stable SEI film, avoiding the entrapment of silicon–lithium alloys during the cycling process. The calculation of the specific capacity is based on the weight of the silicon.

The Si/D/Si/D anode exhibits superior electrochemical reversibility and retains a reversible capacity of 0.11 mAh/cm² (2356 mAh/g (si)) after 100 cycles, which is compared to 0.09 mAh/cm² (1938 mAh/g (si)) for the silicon anode. After 200 cycles, the reversible capacity of the Si/D/Si/D anode was still retained at 0.087 mAh/cm² (1862 mAh/g (si)), with a Coulombic efficiency of 99%, as displayed in Figure 4d. In contrast, the silicon anode shows a reversible capacity of 0.054 mAh/cm² (1159 mAh/g (si)) and a Coulombic efficiency of 98.4%, as shown in Figure 4c. The multi-layer diamond-on-silicon anode has a stable SEI and a uniform ion transportation, thus exhibiting better stability in long-term cycling and a more stable Coulombic efficiency [25,26].

Figure 5a shows a poor cycling performance of the silicon anode and much better cycling performance of the Si/D/Si/D anode. Diamond nanoparticles serve to spread out the lithium ion current and improve the wettability of the silicon anode by the electrolyte, resulting in reduced internal local stress due to non-uniform volume changes by the silicon–lithium alloying and de-alloying processes. The much-improved physical integrity results

in the desirable higher retention of the charge capacity. When the charge–discharge cycle is maintained for two hundred cycles, the improvement in retention is more obvious.

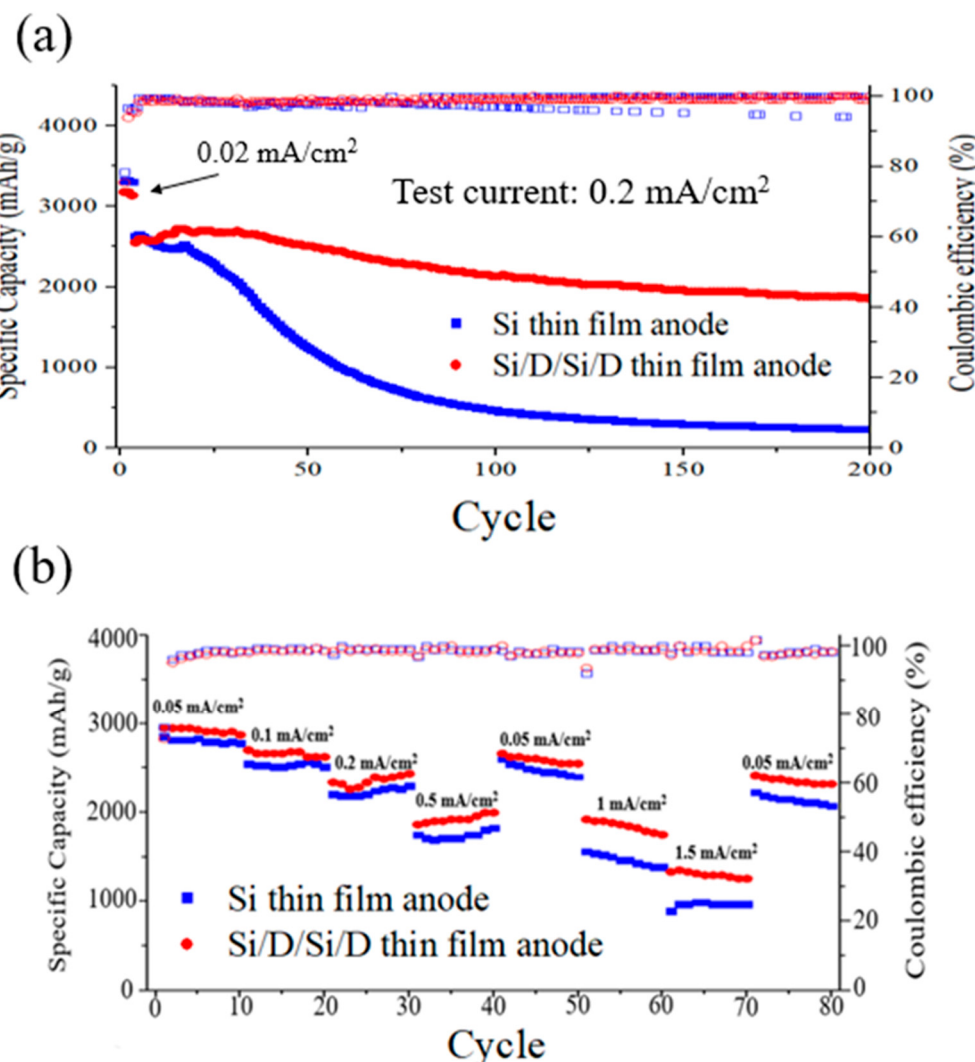


Figure 5. (a) Cycle performance of Si thin-film anode and Si/D/Si/D thin-film anode during the first three cycles of charge and discharge at a current density of $0.02 \text{ mA}/\text{cm}^2$, and for subsequent cycles at a current density of $0.2 \text{ mA}/\text{cm}^2$. (b) C-Rate performance of Si anode and Si/D/Si/D anode.

Figure 5b shows the C-Rate performance of the Si anode and Si/D/Si/D anode. We gradually increased the test current from $0.05 \text{ mA}/\text{cm}^2$ to $0.5 \text{ mA}/\text{cm}^2$. At this point, the specific capacity of the Si/D/Si/D film was approximately 2000 mAh/g(si) , while the silicon anode retained about 1750 mAh/g(si) . When the test current was reduced back to $0.05 \text{ mA}/\text{cm}^2$, the specific capacity of the Si/D/Si/D anode was restored to 2500 mAh/g(si) , and the silicon anode's specific capacity was approximately 2400 mAh/g(si) . We further increased the test current to $1.5 \text{ mA}/\text{cm}^2$ (15 C). Thanks to the uniform ion transportation of the two-layer diamond-on-silicon anode, a specific capacity of about 1350 mAh/g(si) at the equivalent of 15 C was retained. In contrast, the silicon anode only retained a specific capacity of about 1000 mAh/g(si) using the same test current. The uneven charge–discharge process led to structural damages, which degraded the anode performance in the subsequent lower-current tests.

Furthermore, the effectiveness of the surface diamond nanoparticles in uniformly dispersing the charge–discharge current while enhancing the strength of the SEI layer was demonstrated. The diamond-on-silicon anode retained a specific capacity of 1600 mAh/g(si)

after 10 charge–discharge cycles at 1 mA/cm^2 and 1400 mAh/g(si) after 10 charge–discharge cycles at 1.5 mA/cm^2 , both of which were much higher than that of the silicon anode [15,27].

Figure 6a,c show optical microscope surface images of a silicon anode after (a) 200 cycles and (c) 80 cycles of C-rate testing. Figure 6b,d show optical microscope surface images of the Si/D/Si/D anode after completing (b) 200 cycles and (d) 80 cycles of C-rate testing, respectively. For the silicon anode, we observed that in some areas, the silicon film detached from the copper current collector. The overall electrochemical reaction was uneven with more silicon detachment on one side than the other of the electrode. The partial detachment of the silicon film from the current collector was displayed.

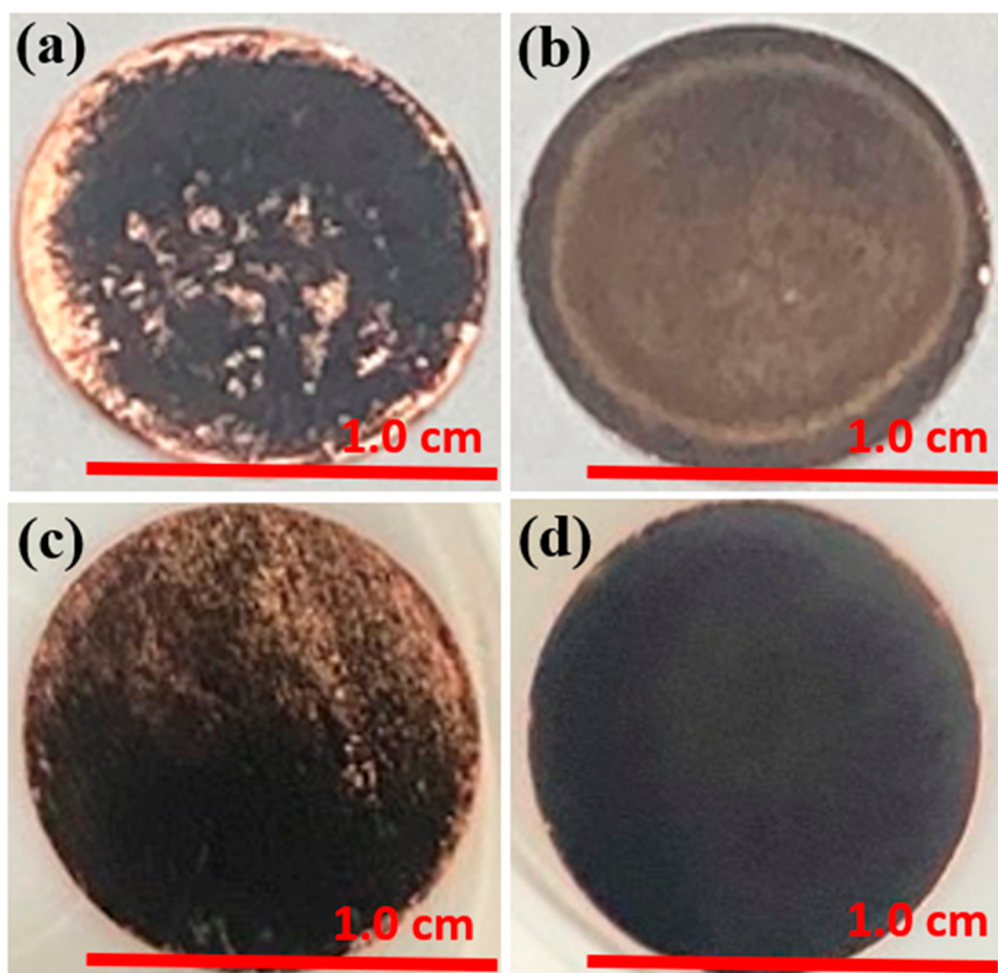


Figure 6. Optical microscope images of (a) Si anode and (b) Si/D/Si/D anode after 200 cycles. (c) Si anode and (d) Si/D/Si/D anode after 80 C-rate testing cycles.

On the other hand, the overall electrode structure of the two-layer diamond-on-silicon anode remained intact after cycling. This confirms that the diamond layers evenly disperse the charge–discharge current, avoiding local excessive reactions, which could lead to local stress and electrode polarization and fracture [27,28].

After a long-term cycling test, the anode surface was characterized using secondary electron microscopy and EDS as shown in Figure 7, to observe changes in the microstructure, elemental composition, and cross-sectional thickness. The formation of separated silicon islands was noted. They might be attributed to the plastic deformation of the copper foil current collector. During cycling, the alloying and de-alloying induced volume changes increased strain and led to the formation of islands with gaps between them. The delamination of silicon from copper was observed. The formation of copper–silicon–lithium

compounds (Cu_2LiSi) during cycling might have weakened the adhesion of silicon to copper, resulting in the delamination of silicon and the loss of electrical contact.

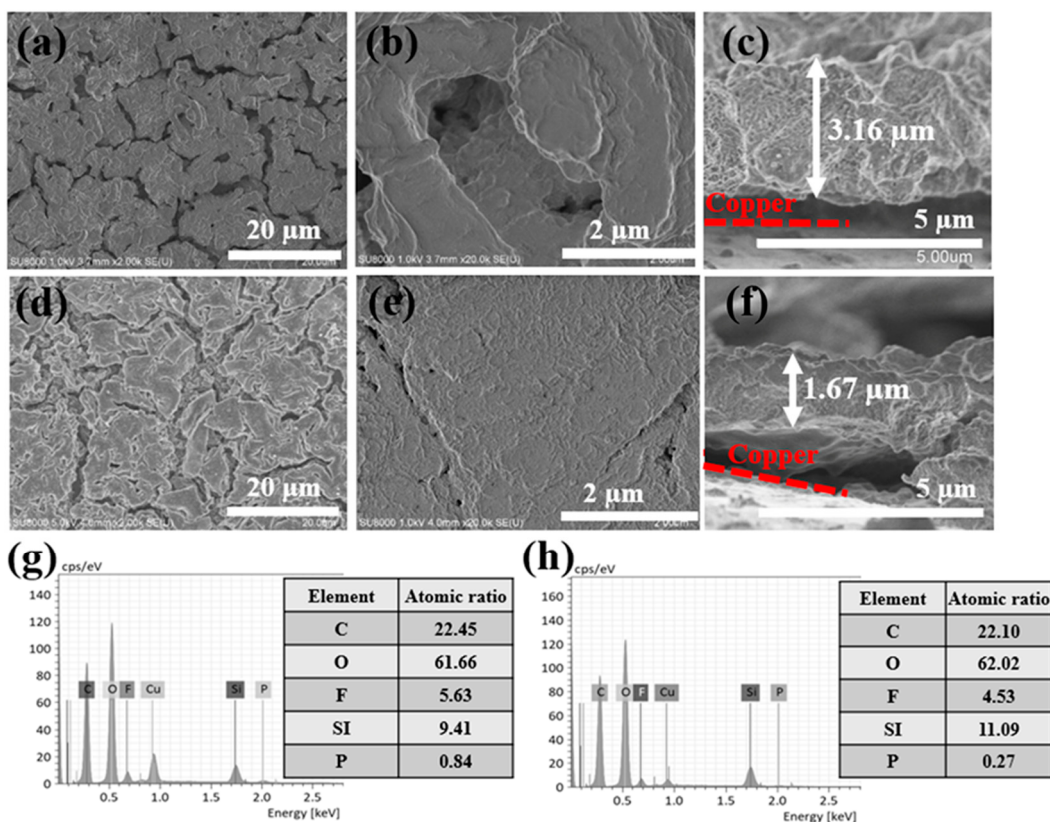


Figure 7. SEM images of (a,b) the surface of Si anode after 200 cycles at different magnification, (c) a cross-section of a Si anode; SEM images of (d,e) the surface of a Si/D/Si/D anode after 200 cycles at different magnification, (f) a cross-section of a Si/D/Si/D anode; EDS analysis of (g) a silicon anode and (h) a Si/D/Si/D anode after 200 cycles.

The surface of the silicon anode exhibited severe roughness and showed numerous protrusions and deep holes in the anode after long-term cycling, indicating uneven reactions in different areas of the anode. This unevenness could partially be attributed to the irregularity of the copper surface or the deposition of uneven silicon films. Without the diamond layer for spreading the lithium transport on the surface area, where a higher lithium ion current density would lead to more alloying and thus a larger volume expansion, non-even volume expansion causes localized stress, which results in cracks to form in the silicon films and the exposure of fresh silicon for the formation of additional SEI layers.

Volume expansion and the build-up of SEI layers caused the anode thickness to increase to nearly 3 μm in some areas of the anode after 200 cycles of the charge–discharge operation. Volume expansion is caused by continuous generation of additional solid electrolyte interphase (SEI). Stress induced by uneven volume expansion might lead to the loss of electrical contacts between the active silicon material and its electrical conductive network. Additionally, the growth of SEI and the increase in the electrical resistance of the anode hindered the rapid diffusion of Li ions and electron conduction, and even trapped some Li irreversibly in the Si anode.

The surface of the silicon anode exhibited a higher phosphorus content than that of the Si/D/Si/D anode. It might originate from phosphates (PO_x), which is the main component of the SEI, or arise from side reactions between the silicon and electrolyte. The remaining fluoride content likely originated from residual electrolyte trapped in the solid electrolyte interphase.

The two-layer diamond-on-silicon thin-film anode displayed a smoother surface and far less of an increase in thickness after cycling than the silicon anode. A more stable solid electrolyte interphase and lower polarization were achieved by the surface layer and the interfacial layer diamond nanoparticles in a thin-film silicon anode for the lithium ion battery [29,30].

X-ray Photoelectron Spectroscopy (XPS) analyses of the chemical composition of both anodes are shown in Figure 8. The concentrations of silicon in the Si anode and the Si/D/Si/D anode are approximately 1.7 and 1.2 atomic %, respectively. Further differences exist in the carbon-to-oxygen ratios and fluorine concentrations. The Si/D/Si/D anode has a higher carbon-to-oxygen ratio of 1.14. Without diamond, the ratio is only 0.52. The fluorine concentration in the Si/D/Si/D anode is higher at 24.7 atomic %, compared to 14.6 atomic % for the silicon anode.

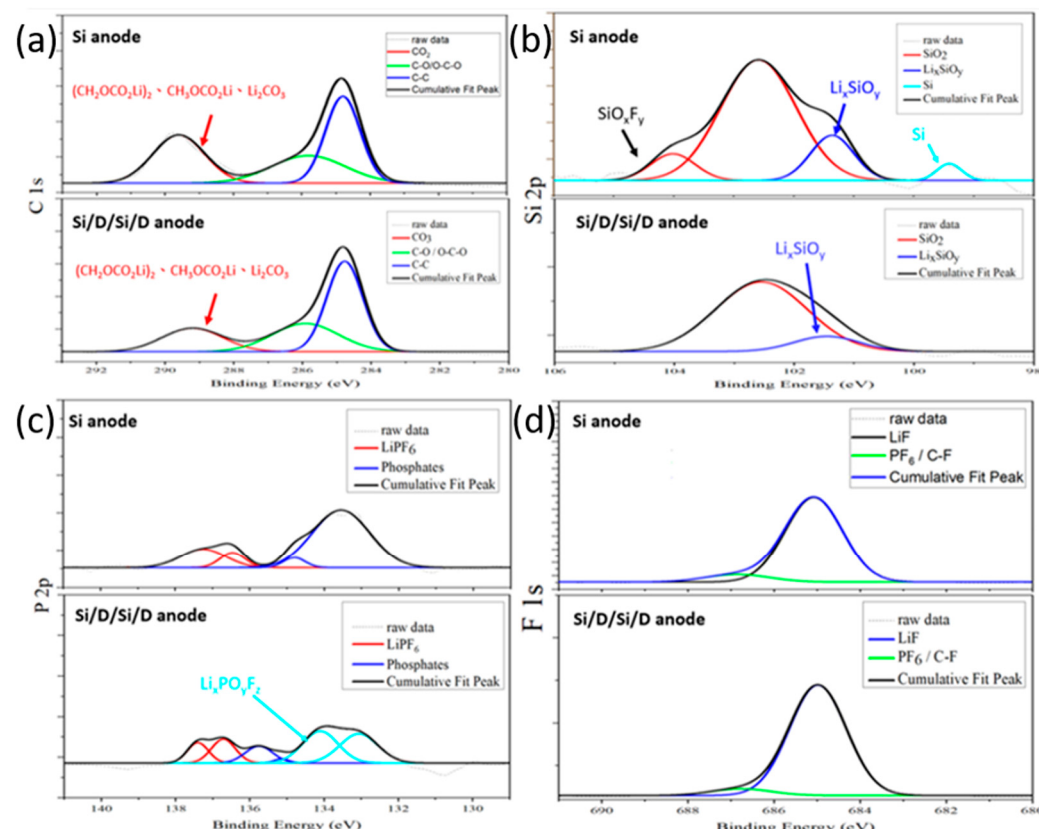


Figure 8. XPS (a) C 1s spectra of Si anode and Si/D/Si/D anode; (b) Si 2p spectra of Si anode and Si/D/Si/D anode, SiO_2 has two bands shown in red color; (c) P 2p spectra of Si anode and Si/D/Si/D anode; and (d) F 1s spectra of Si anode and Si/D/Si/D anode after 200 cycles of discharge and charge operation.

These results indicate that the application of diamond nanoparticles in the Si/D/Si/D anode affects the compositional contents of the solid electrolyte interphase (SEI), leading to higher concentrations of carbon and fluorine. This also suggests a significant impact of nano-diamonds (NDs) on the decomposition, regeneration, and build-up processes of the SEI, potentially influencing the cycling performance and the stability of lithium-ion batteries.

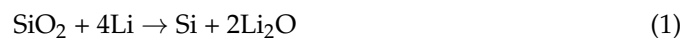
The carbon spectral results reveal that SEI components are located mainly near the anode surface of the silicon anode after long-term cycling. This indicates the more rapid consumption of the electrolyte.

The silicon spectra show that there is a stronger signal of silicon on the surface of the silicon anode, indicating that the SEI layer cracks repetitively during the charge and

discharge process, leading to the continuous exposure of fresh silicon surfaces, which would cause the build-up of additional SEI.

After cycling, the characteristic value of the binding energy for the C 1s peak is maximized at 284.8 eV, mainly corresponding to the C-C and C-H bonds, as shown in Figure 8a. The second local maximum is at 289.7 eV, which is due to lithium carbonate and different semi-organic lithium carbonate. These results demonstrate the presence of typical SEI components such as $(\text{CH}_2\text{OCO}_2\text{Li})_2$, $\text{CH}_3\text{OCO}_2\text{Li}$, CH_3OLi , and Li_2CO_3 in the alkyl carbonate. The signal intensity is proportional to the degree of electrolyte decomposition. For the Si/D/Si/D anode, the main signal shifts to 289.2 eV, which proves that the SEI layer on this anode is thinner [29].

The Si 2p spectra in Figure 8b show signals with maxima at around 101 eV, which corresponds to Li_xSiO_y . It is the initial reaction product of lithium with SiO_2 . SiO_2 is present in a higher concentration on the original anode. HF is a by-product of the decomposition reaction of PF_6^- ions with trace amounts of water and FEC additives. It can be clearly seen from reactions (1)–(3) that a large amount of Li_2O and Li_4SiO_4 are formed [31]. For the silicon anode, we observed a shoulder peak at 105 eV, corresponding to fluorinated silicon suboxide (SiO_xF_y) [31,32].



The P2p spectrum in Figure 8c shows a binding energy of 134.0 eV, proving that mainly phosphates and fluorine-substituted phosphates are present. The presence of FEC leads to the hydrolyzing of a large amount of LiPF_6 into (fluorinated) phosphates, which are integrated into the inorganic part of the SEI. The general reaction path for phosphate formation has been described in the literature [32]. Therefore, more water is generated in the Si/D/Si/D anode. This is probably due to the reaction of silicon and Li_2O with HF. Similar results were reported by Elazari et al. [33]. Hydrolysis is considered the main factor for the irreversible capacity loss in LIBs, but it appears to have a positive effect on the electrochemical performance. This behavior is consistent with the report by Dalavi et al., who observed a positive effect on the electrochemical performance when decomposed LiPF_6 was included in the SEI [34].

The F 1s spectra of both anodes shown in Figure 8d are composed of low-intensity signals at 687.7 eV and a significant signal at 685.5 eV. These are from trace amounts of LiPF_6 , $\text{Li}_x\text{PO}_y\text{F}_z$, and LiF . The phosphorus species can be confirmed by the P 2p spectrum (see Figure 8c). The signal at 137.5 eV indicates trace amounts of conductive salts, while the signal at 134.5 eV points to partially fluorinated phosphates. The presence of fluorinated phosphates after cycling in conventional carbonate electrolytes as parts of the SEI was reported [32,35].

Figure S1 shows that the crystalline diamond nanoparticles of 3.6 nm adhering on the surface of a silicon thin film improves its hydrophilicity for the uniform wetting of the anode by the electrolyte. Uniform SEI growth on the electrode and the current spreading effects of diamond nanoparticles, due to the slow diffusion of lithium through diamond, are attributed to the prevention of excessive internal stress due to uneven volume expansion across the anode and a smaller increase in anode thickness after 200 cycles of charge-discharge operation. The damages to the anode with diamond nanoparticles are thus reduced and the much better cycling life time and capacity retention are achieved by the Si/D/Si/D anode in comparison with the pure silicon anode. This is further confirmed by the significantly smaller electrochemical impedance enabled by diamond nanoparticles, as shown in Figure S2 and Table S1. Cycling performance of additional silicon–diamond structures are presented in Figure S3.

4. Conclusions

We have discovered that the surface and interfacial layers of single-crystal diamond nanoparticles significantly improve the performance of thin-film silicon-based anodes for lithium-ion batteries. Diamond nanoparticles of 3.6 nm-sized crystals adhere to silicon thin films in the ambient environments without needing vacuum-based diamond CVD processes. The double-layer Si/D/Si/D anode exhibits the uniform alloying of the silicon with lithium and the formation of SEI on the surface, reducing the internal stress and preventing the anode from fracture and pulverization. It results in the desired physical integrity of the anode, including a more stable SEI layer. Significant improvements in the electrochemical stability and reversible capacity retention under high-rate and long-term cycling conditions were demonstrated in comparison with the thin-film silicon anode without diamond additives. The X-ray photoelectron spectroscopy (XPS) analysis reveals that the addition of crystalline nano-diamonds (NDs) leads to the composition of the SEI to contain more carbon and fluorine. This indicates that crystalline nano-diamonds (NDs) play important roles in the decomposition and regeneration processes of the SEI. A facile process of adhering crystalline diamond nanoparticles on thin-film silicon surfaces as an anode material with significantly improved cycling performance for lithium-ion batteries has been reported.

Supplementary Materials: The following supporting information can be downloaded at: <https://www.mdpi.com/article/10.3390/batteries10090321/s1>, Figure S1: Water on anode surface for comparison in hydrophilicity of Si thin-film anode and Si/D/Si/D thin-film anode [36]; Figure S2: Electrochemical impedance spectra of Si thin-film anode and Si/D/Si/D thin-film anode after the 200th electrochemical cycling: (a) typical Nyquist plot; (b) the equivalent circuit used to fit impedance data. R₁ is the cell internal resistance. R₂ is the charge transfer resistance. CPE is the double-layer pseudo-capacity. Warburg Element is the solid-state diffusion element [37]; Figure S3: Cycling performance of Si, Si/D/Si, Si/D/Si/D, and Si/D/Si/D/Si/D thin-film anode under test current 0.05 mA/cm². Table S1: Parameter values of equivalent circuits based on EIS spectra of anodes of Si thin film and Si/D/Si/D thin film after 200 cycles of charge–discharge.

Author Contributions: Y.T.: Conception, funding, data analysis, interpretation, final manuscript preparation; C.-Y.J.: Material characterization, data analysis, draft manuscript preparation; S.-H.S.: Device fabrication, data collection, initial data analysis, report preparation; Y.-Y.C.: Experimental assistance, data collection and verification, assistance to report preparation. All authors have read and agreed to the published version of the manuscript.

Funding: This work is partially supported by the National Science and Technology Council in Taiwan under the grant number NSTC-112-2221-E-006-075-.

Data Availability Statement: No new data were created.

Acknowledgments: The authors gratefully acknowledge the use of the scanning electron micro-scope (SEM, Hitachi-SU8000, Taipei, Taiwan) and X-ray Photoelectron Spectrometer (PHI Versa Probe 4, Taipei, Taiwan) belonging to the Core Facility Center of the National Cheng Kung University.

Conflicts of Interest: The authors declare that they have no competing financial interests or personal relationships that appear to have influenced the work reported in this paper.

References

- Li, L.; Wu, Z.; Yuan, S.; Zhang, X.B. Advances and challenges for flexible energy storage and conversion devices and systems. *Energy Environ. Sci.* **2014**, *7*, 2101–2122. [[CrossRef](#)]
- Thackeray, M.M.; Wolverton, C.; Isaacs, E.D. Electrical energy storage for transportation—Approaching the limits of, and going beyond, lithium-ion batteries. *Energy Environ. Sci.* **2012**, *5*, 7854–7863. [[CrossRef](#)]
- Bai, S.; Chen, S.; Shen, X.; Zhua, G.; Wang, G. Nanocomposites of hematite (α -Fe₂O₃) nanospindles with crumpled reduced graphene oxide nanosheets as high-performance anode material for lithium-ion batteries. *RSC Adv.* **2012**, *2*, 10977–10984. [[CrossRef](#)]
- Ge, M.; Cao, C.; Biesold, G.M.; Sewell, C.D.; Hao, S.M.; Huang, J.; Lin, Z. Recent advances in silicon-based electrodes: From fundamental research toward practical applications. *Adv. Mater.* **2021**, *33*, 2004577. [[CrossRef](#)] [[PubMed](#)]

5. Li, L.; Deng, Y.; Hu, K.; Xu, B.; Wang, N.; Bai, Z.; Yang, J. Nanostructure designing and hybridizing of high-capacity silicon-based anode for lithium-ion batteries. *Prog. Nat. Sci. Mater. Int.* **2023**, *33*, 16–36. [[CrossRef](#)]
6. Chen, X.; Li, H.; Yan, Z.; Cheng, F.; Chen, J. Structure design and mechanism analysis of silicon anode for lithium-ion batteries. *Sci. China Mater.* **2019**, *62*, 1515–1536. [[CrossRef](#)]
7. Kim, H.; Seo, M.; Park, M.H.; Cho, J. A critical size of silicon nano-anodes for lithium rechargeable batteries. *Angew. Chem. Int. Ed.* **2010**, *49*, 2146–2149. [[CrossRef](#)]
8. Wu, H.; Cui, Y. Designing nanostructured Si anodes for high energy lithium ion batteries. *Nano Today* **2012**, *7*, 414–429. [[CrossRef](#)]
9. Liu, L.; Lyu, J.; Li, T.; Zhao, T. Well-constructed silicon-based materials as high-performance lithium-ion battery anodes. *Nanoscale* **2016**, *8*, 701–722. [[CrossRef](#)]
10. Jiang, S.; Hu, B.; Sahore, R.; Zhang, L.; Liu, H.; Zhang, L.; Zhang, Z. Surface-functionalized silicon nanoparticles as anode material for lithium-ion battery. *ACS Appl. Mater. Interfaces* **2018**, *10*, 44924–44931. [[CrossRef](#)]
11. Zamfir, M.R.; Nguyen, H.T.; Moyen, E.; Lee, Y.H.; Pribat, D. Silicon nanowires for Li-based battery anodes: A review. *J. Mater. Chem. A* **2013**, *1*, 9566–9586. [[CrossRef](#)]
12. Wen, Z.; Lu, G.; Mao, S.; Kim, H.; Cui, S.; Yu, K.; Chen, J. Silicon nanotube anode for lithium-ion batteries. *Electrochim. Commun.* **2013**, *29*, 67–70. [[CrossRef](#)]
13. Salah, M.; Murphy, P.; Hall, C.; Francis, C.; Kerr, R.; Fabretto, M. Pure silicon thin-film anodes for lithium-ion batteries: A review. *J. Power Sources* **2019**, *414*, 48–67. [[CrossRef](#)]
14. Tong, L.; Wang, P.; Chen, A.; Qiu, F.; Fang, W.; Yang, J.; Wang, C.; Yang, Y. Improved Electrochemical Performance of Binder-Free Multi-Layered Silicon/Carbon Thin Film Electrode for Lithium-Ion Batteries. *Carbon* **2019**, *153*, 592–601. [[CrossRef](#)]
15. Chen, Y.X.; Liao, H.C.; Cheng, Y.W.; Huang, J.H.; Liu, C.P. Scalable Interlayer Nanostructure Design for High-Rate (10C) Submicron Silicon-Film Electrode by Incorporating Silver Nanoparticle. *ACS Appl. Mater. Interfaces* **2023**, *15*, 18845–18856. [[CrossRef](#)] [[PubMed](#)]
16. Jhan, C.-Y.; Sung, S.-H.; Tzeng, Y. Silicon–Nanodiamond-Based Anode for a Lithium-Ion Battery. *Nanomaterials* **2024**, *14*, 43. [[CrossRef](#)]
17. Jhan, C.-Y.; Wang, P.-S.; Sung, S.-H.; Tzeng, Y. Effects of volume-confinement on lithium-ion battery with silicon-based anode. *Mater. Today Commun.* **2024**, *39*, 108578. [[CrossRef](#)]
18. Tzeng, Y.; Jhan, C.Y.; Wu, Y.H. Effects of pyrolysis on high-capacity Si-based anode of lithium ion battery with high coulombic efficiency and long cycling life. *Nanomaterials* **2022**, *12*, 469. [[CrossRef](#)]
19. Tzeng, Y.; Jhan, C.Y.; Chiu, K.M.; Wu, Y.C.; Chen, G.Y.; Wang, P.S. Si–Ni-alloy-assisted very high-areal-capacity silicon-based anode on Ni foam for lithium ion battery. *Mater. Today Chem.* **2023**, *30*, 101570. [[CrossRef](#)]
20. Tzeng, Y.; Jhan, C.Y.; Wu, Y.C.; Chen, G.Y.; Chiu, K.M.; Guu SY, E. High-ICE and high-capacity retention silicon-based anode for lithium-ion battery. *Nanomaterials* **2022**, *12*, 1387. [[CrossRef](#)]
21. Marcins, G.; Butikova, J.; Tale, I.; Polyakov, B.; Kalendárková, R.; Muhin, A. Crystallization processes of amorphous Si by thermal annealing and pulsed laser processing. *IOP Conf. Ser. Mater. Sci. Eng.* **2011**, *23*, 012035. [[CrossRef](#)]
22. Becker, C.; Dogan, P.; Ruske, F.; Gorka, B.; Sánchez-Vicens, A.; Conrad, E.; Hüpkens, J. Solid phase crystallized silicon thin-film solar cells on temperature-stable ZnO: Al contact layers. In Proceedings of the 23rd European Photovoltaic Solar Energy Conference, Valencia, Spain, 1–5 September 2008; pp. 2045–2048.
23. Lee, S.H.; Choi, M.; Jung, Y.I.; Sim, S.J.; Moon, J.K.; Choi, J.; Kim, S. Deposition and characterization of silicon thin film on stainless steel by electron beam evaporation. *Thin Solid Films* **2022**, *756*, 139380. [[CrossRef](#)]
24. Wang, J.W.; He, Y.; Fan, F.; Liu, X.H.; Xia, S.; Liu, Y.; Zhu, T. Two-phase electrochemical lithiation in amorphous silicon. *Nano Lett.* **2013**, *13*, 709–715. [[CrossRef](#)]
25. Adhitama, E.; Van Wickeren, S.; Neuhaus, K.; Frankenstein, L.; Demelash, F.; Javed, A.; Placke, T. Revealing the role, mechanism, and impact of AlF₃ coatings on the interphase of silicon thin film anodes. *Adv. Energy Mater.* **2022**, *12*, 2201859. [[CrossRef](#)]
26. Tong, L.; Wang, P.; Fang, W.; Guo, X.; Bao, W.; Yang, Y.; Qiu, F. Interface engineering of silicon/carbon thin-film anodes for high-rate lithium-ion batteries. *ACS Appl. Mater. Interfaces* **2020**, *12*, 29242–29252. [[CrossRef](#)] [[PubMed](#)]
27. Tamirat, A.G.; Lui, Y.; Dong, X.; Wang, C.; Wang, Y.; Xia, Y. Ultrathin Silicon Nanolayer Implanted Ni_xSi/Ni Nanoparticles as Superlong-Cycle Lithium-Ion Anode Material. *Small Struct.* **2021**, *2*, 2000126. [[CrossRef](#)]
28. Mukanova, A.; Jetybayeva, A.; Myung, S.T.; Kim, S.S.; Bakenov, Z. A mini-review on the development of Si-based thin film anodes for Li-ion batteries. *Mater. Today Energy* **2018**, *9*, 49–66. [[CrossRef](#)]
29. Jaumann, T.; Balach, J.; Klose, M.; Oswald, S.; Langklotz, U.; Michaelis, A.; Giebel, L. SEI-component formation on sub 5 nm sized silicon nanoparticles in Li-ion batteries: The role of electrode preparation, FEC addition and binders. *Phys. Chem. Chem. Phys.* **2015**, *17*, 24956–24967. [[CrossRef](#)]
30. Aryanfar, A.; Brooks, D.J.; Colussi, A.J.; Hoffmann, M.R. Quantifying the dependence of dead lithium losses on the cycling period in lithium metal batteries. *Phys. Chem. Chem. Phys.* **2014**, *16*, 24965–24970. [[CrossRef](#)]
31. Philippe, B.; Dedryvère, R.; Allouche, J.; Lindgren, F.; Gorgoi, M.; Rensmo, H.; Edström, K. Nanosilicon electrodes for lithium-ion batteries: Interfacial mechanisms studied by hard and soft X-ray photoelectron spectroscopy. *Chem. Mater.* **2012**, *24*, 1107–1115. [[CrossRef](#)]
32. Philippe, B.; Dedryvère, R.; Gorgoi, M.; Rensmo, H.; Gonbeau, D.; Edström, K. Role of the LiPF₆ salt for the long-term stability of silicon electrodes in Li-ion batteries—A photoelectron spectroscopy study. *Chem. Mater.* **2013**, *25*, 394–404. [[CrossRef](#)]

33. Elazari, R.; Salitra, G.; Gershinsky, G.; Garsuch, A.; Panchenko, A.; Aurbach, D. Li ion cells comprising lithiated columnar silicon film anodes, TiS_2 cathodes and fluoroethylene carbonate (FEC) as a critically important component. *J. Electrochem. Soc.* **2012**, *159*, A1440. [[CrossRef](#)]
34. Dalavi, S.; Guduru, P.; Lucht, B.L. Performance enhancing electrolyte additives for lithium ion batteries with silicon anodes. *J. Electrochem. Soc.* **2012**, *159*, A642. [[CrossRef](#)]
35. Etacheri, V.; Haik, O.; Goffer, Y.; Roberts, G.A.; Stefan, I.C.; Fasching, R.; Aurbach, D. Effect of fluoroethylene carbonate (FEC) on the performance and surface chemistry of Si-nanowire Li-ion battery anodes. *Langmuir* **2012**, *28*, 965–976. [[CrossRef](#)]
36. Sun, X.; Wang, C.; Zhang, X.; Zhai, X.; Feng, J.; Li, H. Nanodiamond-modified separators and optimized graphene anodes for highly enhanced performance of lithium-ion batteries. *J. Alloys Compd.* **2022**, *929*, 167204. [[CrossRef](#)]
37. Wu, J.J.; Bennett, W.R. Fundamental investigation of Si anode in Li-ion cells. In Proceedings of the 2012 IEEE Energytech, Cleveland, OH, USA, 29–31 May 2012; pp. 1–5.

Disclaimer/Publisher's Note: The statements, opinions and data contained in all publications are solely those of the individual author(s) and contributor(s) and not of MDPI and/or the editor(s). MDPI and/or the editor(s) disclaim responsibility for any injury to people or property resulting from any ideas, methods, instructions or products referred to in the content.